Viscoelasticity and interface properties of multi-component condensates govern protein sequestration and suppression of amyloid formation

Tharun Selvam Mahendran[1]†, Anne Bremer[2]†, Xinrui Gui[2]†, Anurag Singh[3], Joseph L. Basalla[3], Sagar Chittori[2], Melissa R. Marzahn[2], Tapojyoti Das[2], Tanja Mittag[2]*, Priya R. Banerjee[1,3]*

[1] Department of Biological Sciences, The State University of New York at Buffalo; Buffalo, NY, USA.

[2] Department of Structural Biology, St. Jude Children's Research Hospital; Memphis, TN, USA.

[3] Department of Physics, The State University of New York at Buffalo; Buffalo, NY, USA.

*Correspondence should be addressed to: PRB (prbanerj@buffalo.edu) and TM (tanja.mittag@stjude.org).

† These authors contributed equally to this work.

Abstract

Stress granules (SGs) are multi-component protein–RNA condensates widely viewed as crucibles for fibril formation in neurodegenerative diseases such as amyotrophic lateral sclerosis. Here, we test this model by examining whether SG-mimics promote or suppress amyloid formation. Using multi-component programmable peptide–nucleic acid condensates, we show that condensates delay amyloid assembly by sequestering soluble proteins, and that fibrils grow in the dilute phase. Systematic tuning of condensate material properties reveals two key modulating mechanisms: the density of fibril-forming proteins at condensate interfaces dictates the lag phase of fibril assembly, and condensate viscoelasticity regulates protein efflux–driven fibril growth. These principles extend to SG-mimic condensates formed by G3BP1 and RNA, suggesting that SGs may function as potent suppressors rather than crucibles of pathological amyloid assembly.

Stress-responsive phase separation of G3BP1/G3BP2 and other RNA-binding proteins (RBPs) with untranslated mRNAs mediates the formation of stress granules (SGs) and is important for cell survival (*1-6*). Yet, multiple lines of genetic, histopathological, and cell-biological evidence suggest that the prolonged assembly of SGs drives the pathogenesis of neurodegenerative diseases such as amyotrophic lateral sclerosis, frontotemporal dementia, and multisystem proteinopathy (*7-10*). The shared pathological hallmark of these diseases is the presence of solid, fibrillar deposits formed by specific RBPs in patient cells. Because fibril-forming RBPs such as hnRNPA1, TIA1, FUS, and TDP-43 are enriched in SGs, these assemblies are often regarded as potential sites (*11*), or even crucibles (*12*), for amyloid fibril formation (*13*). The link between SGs and protein fibril formation is supported by the fact that fibrils typically appear at the sites of condensates *in vitro*, an observation that has been interpreted to indicate that the high local concentration of protein in condensates promotes nucleation and feeds growth of fibrils (*14-16*). Furthermore, fibrils appear earlier in samples containing condensates than in samples without condensates (*16*). These insights have led to a model where SGs are thought to promote fibril formation. By contrast, certain cell biological lines of evidence support a contrasting view that SGs may be protective. For example, TDP-43 is relatively better protected against aggregation when located in SGs than in other types of condensates (*17*). Furthermore, pathological inclusions of cytoplasmic TDP-43 can arise independently of SGs, suggesting that protein aggregation may proceed more readily in the so-called dilute phase outside condensates (*18-20*).

Our recent characterization of the influence of phase separation of the prion-like low-complexity domain (LCD) of hnRNPA1 (A1-LCD) on its fibril formation suggested that the interiors of condensates can suppress fibril formation by sequestering soluble protein (*21*). However, some aspects of these homotypic condensates can nevertheless promote fibril formation. For example, the condensate interfaces can accelerate fibril nucleation (*21-24*), explaining earlier observations that fibrils appear earlier in the presence of condensates (*16*) and are apparently attached to them (*15*). In contrast to previous interpretations, we found that fibrils grow in the dilute phase, and that condensates are metastable sinks that limit fibril growth by reducing protein concentrations in the dilute phase and by slowing protein efflux from the dense phase (*21*). However, the use of a mono-component system in which the same fibril-forming protein also drives condensate formation limits insights into the implications for SGs, which are inherently multi-component assemblies.

These recent insights into the opposing roles of condensates via their interiors and interfaces raise several fundamental questions that must be addressed to understand the role of SGs in neurodegenerative diseases and generate effective interventions. (1) Do multi-component condensates that resemble SGs (i.e., SG mimics) enhance or suppress fibril formation? (2) Is the presence of heterotypic interactions in multi-component condensates more effective in inhibiting fibril-promoting interactions relative to mono-component, homotypic condensates, a concept previously proposed as “heterotypic buffering” (*25*)? (3) Do condensate interiors and interfaces play opposing roles in multi-component SG mimics, or do multi-component systems also enable suppression of fibril formation at interfaces? (4) Driving forces for phase separation, viscoelasticity, and condensate metastability are typically strongly interrelated (*26*). Do multi-component systems allow us to disentangle how distinct condensate properties, such as viscoelasticity, protein sequestration, and transport across the condensate interface, contribute to the regulation of fibril formation?

Herein, we leverage multi-component peptide–nucleic acid condensates whose components are facsimiles of relevant SG building blocks, and which have programmable physical properties, to characterize systematically, quantitatively, and mechanistically how multi-component condensates influence amyloid formation of a protein that is implicated in neurodegenerative diseases. SGs host an intricate network of homotypic and heterotypic interactions between nucleic acids and proteins containing LCDs (*27*). Among distinct LCDs,

prion-like domains (PLDs) and arginine/glycine-rich repeat (RGG) domains are of interest due to their large abundance in the SG proteome (*27-30*). Some PLD-containing proteins carry disease-related mutations and form fibrillar inclusions in patients (*31*). The D262V mutation in hnRNPA1 causes highly penetrant disease in affected families (*31*). Therefore, we selected the wild-type (WT) A1-LCD and its pathogenic mutant, D262V, as the fibril-forming proteins of interest. To mimic the SG microenvironment, we employed RGRGG-repeat peptides, which, together with single-stranded DNA or RNA, form condensates that favorably recruit A1-LCD. By making subtle changes to the peptide sequence or the nucleic acid chain length, we tune the viscoelastic properties of the resulting condensates by nearly three orders of magnitude, enabling the mechanistic dissection of their effects on A1-LCD fibril formation. Lastly, we test whether our insights are generalizable to condensates formed by the major SG hub protein G3BP1, which does not form fibrils itself but phase separates with untranslated, poly-adenylated mRNA, which we mimic using poly-A RNA (*2, 6*). These condensates recruit the fibril-forming A1-LCD and can complement our insights as superior, albeit less tunable, mimics of SGs. Our results demonstrate that G3BP1-RNA condensates suppress fibril formation of A1-LCD via multiple SG-inherent properties, providing direct evidence that SGs may not be crucibles for neurodegenerative disease but instead protect against fibril formation of proteins that preferentially partition into them.

Protein fibrils grow in the dilute phase

We recently showed that metastable condensates formed by the PLD of hnRNPA1 (A1-LCD) serve as sinks for soluble protein and kinetically suppress their conversion to fibrils (*21*). We asked whether SG-mimic, multi-component condensates formed by nucleic acids and peptides containing multivalent RGG-domains, similarly suppress fibril formation of A1-LCD. Specifically, we used condensates formed by single-stranded (ss) poly-thymine DNA (dT_{40}) and a multivalent R/G-rich polypeptide [$(RGRGG)_5$] (*32*) as a model system to mimic the heterotypic SG microenvironment (**Fig. 1A**). One key advantage of this multi-component condensate system is that it offers precise control over condensate viscoelasticity through peptide sequence design (*32*) and nucleic acid chain length (*33*) and can thus be employed to ask how physical properties of condensates influence recruitment and fibril formation of A1-LCD (**Fig. 1A, Tables S1-S3**).

WT A1-LCD and D262V partition favorably into condensates formed by RGRGG-repeat peptide and dT_{40} ssDNA (**Fig. 1B**). To assess whether these condensates promote or suppress fibril formation, we progressively increased the concentrations of condensate-forming components, peptide and ssDNA, while keeping the A1-LCD concentration constant. We monitored A1-LCD fibril formation through changes to the fluorescence intensity of Thioflavin T (ThT), a dye whose fluorescence intensity increases strongly when it binds to amyloid fibrils (*34*). Samples with peptide–ssDNA condensates without A1-LCD remained ThT-negative (**Fig. 1C**). In the absence of condensates, A1-LCD formed fibrils rapidly, as evidenced by a sigmoidal ThT curve with a lag time ($t_{5\%}$, which we defined as the time to reach 5% of the ThT plateau value) of ~1.5 hours (**Fig. 1C, D**). Fibrils were also directly visualized by negative-stain transmission electron microscopy (nsTEM; **Fig. 1E**). Increasing the concentrations of peptide and ssDNA at constant A1-LCD concentration increased the lag time progressively (**Fig. 1C, D**). Considering that ThT binding is subject to variation across different fibrillar species, we did not quantitatively analyze the slopes and plateau values of the ThT curves; instead, we used the lag time as an empirical parameter to deduce the time required for the onset of fibril assembly across samples. Observation of the process using brightfield microscopy confirmed that the formation of detectable mesoscale aggregates was increasingly suppressed (**Fig. 1F**). The peptide–ssDNA condensates similarly delayed the formation of fibrils of the pathogenic mutant A1-LCD D262V (**Fig. S1A-D**). Taken together, these results show that partitioning of the fibril-forming protein into multi-

component condensates suppresses fibril formation.

We note that observations by light microscopy and nsTEM are seemingly at odds: While ThT kinetics and nsTEM demonstrate the rapid appearance of fibrils in samples without condensates (**Fig. 1C, E**), light microscopy can detect fibrillar structures only in samples that contain condensates (**Fig. 1F**). The diameter of single amyloid fibrils is typically too small to be detectable by light microscopy, and we therefore speculate that fibrils are bundled in the presence of condensates, enabling their visualization by light microscopy. These observations demonstrate the challenge of elucidating the underlying processes comprehensively through diffraction-limited light microscopy and point to the requirement of integrating complementary measurements.

To test whether fibril formation kinetics are dampened by progressive sequestration of A1-LCD into condensates as peptide and ssDNA concentrations are increased, we determined dilute phase concentrations (c_{dilute}) of A1-LCD in the presence of condensates using analytical HPLC measurements (*35*) (**Fig. 1G**; *see* Methods). At 62.5 μg/mL peptide and ssDNA, c_{dilute} of A1-LCD was 5.4 μM, whereas it was reduced to 1.6 μM at 125 μg/mL peptide/ssDNA concentrations (**Fig. 1H**). c_{dilute} of A1-LCD was below the detection limit at higher than 125 μg/mL peptide/ssDNA concentrations. These data suggest that A1-LCD is progressively sequestered into the condensates at increasing peptide and ssDNA concentrations, thereby protecting against A1-LCD fibril formation (**Fig. 1F**).

Based on these observations, we hypothesized that fibril growth predominantly occurs in the dilute phase. To directly test this idea, we used time-lapse confocal fluorescence microscopy and monitored the spatial distribution of fluorescently labeled RGRGG-repeat peptide and the ThT signal in condensates. In the absence of A1-LCD protein, the condensates did not show any ThT signal above the background level (**Fig. 1I**). Condensate samples containing A1-LCD D262V after 8 hours of incubation resulted in a prominent ThT signal at the perimeter of condensates, and ThT-positive fibrillar structures extended into the dilute phase (**Fig. 1I**). To test if any fibrils were detectable in the dense phase, we performed confocal Z-stack imaging, which revealed that the fibrils localize in the dilute phase (**Fig. 1J, K, Video S1**). Utilizing a near-infrared amyloid reporter dye, CRANAD2, and Alexa488-labeled A1-LCD D262V simultaneously, we confirmed that the fibrillar structures at the condensate perimeter are indeed formed by A1-LCD (**Fig. S1E**). Overall, our observations suggest that A1-LCD fibrils do not form in condensate interiors. These findings contrast with the prevailing view that fibril formation occurs in condensates owing to the high local concentration of fibril-forming protein within them (*36, 37*), but are in agreement with studies that used homotypic condensates of A1-LCD variants (*21*) and Tau (*38*), which showed that condensates suppress fibril formation and that fibrils form in the dilute phase.

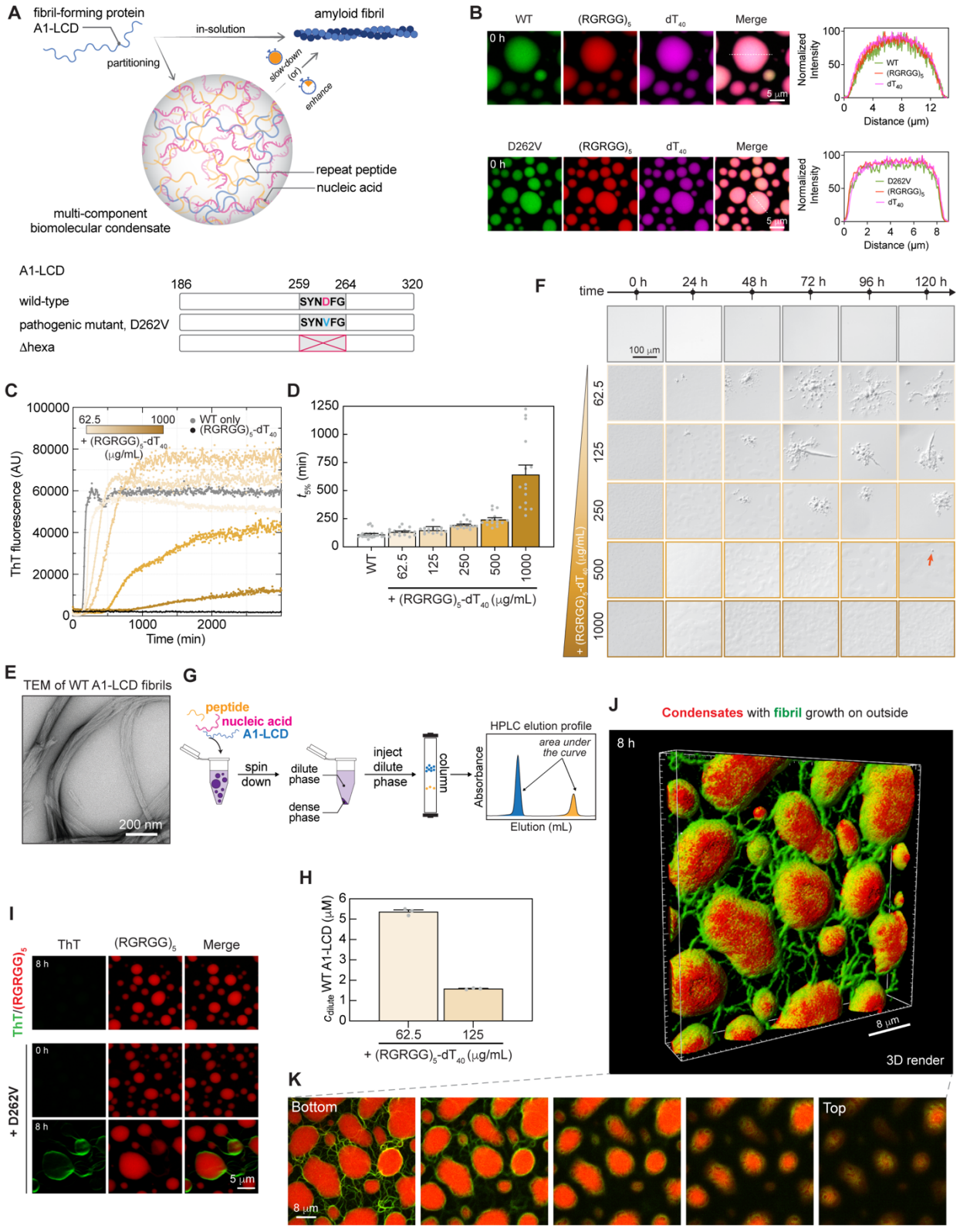

Figure 1. Multi-component biomolecular condensates suppress A1-LCD fibril formation. (A) (top) Schematic of the experimental system designed to test whether multi-component peptide–nucleic acid condensates accelerate or suppress fibril formation kinetics. (bottom) Schematic highlighting the sequence

architecture and steric zipper motif (represented as a grey rectangle) of wild-type (WT) A1-LCD, encompassing residues 186 to 320 of the full-length hnRNPA1 protein, and variants of A1-LCD: D262V, a pathogenic mutant, and Δhexa, a variant lacking the steric zipper. **(B)** Fluorescence images and corresponding line profiles show partitioning of either WT A1-LCD (top) or D262V (bottom) [visualized with 250 nM Alexa488-labeled A1-LCD variant] into $(RGRGG)_5$–dT_{40} condensates [visualized with 250 nM Alexa594-$(RGRGG)_5$ and Cy5-dT_{40}]. '0 h' hereafter refers to 15 minutes after sample preparation. **(C)** Kinetics of fibril formation monitored by Thioflavin T (ThT) fluorescence of 25 μM WT A1-LCD either alone or in the presence of increasing concentrations of $(RGRGG)_5$ and dT_{40}. A negative control showing ThT kinetics of $(RGRGG)_5$–dT_{40} condensates in the absence of A1-LCD is also included. A smoothing window of 10 data points was applied to generate a connecting line. **(D)** Lag times ($t_{5\%}$) extracted from the ThT kinetics shown in (C) represent the time required to reach 5% of the plateau ThT fluorescence intensity. Lag times from replicate experiments ($n \geq 3$) are shown along with the mean ± standard error of the mean (SEM). **(E)** Negative-stain transmission electron microscopy (nsTEM) image of A1-LCD fibrils from samples without condensates captured after 6 days of incubation at 20 ℃ with shaking. **(F)** Time course of differential interference contrast (DIC) images of WT A1-LCD alone, and in the presence of increasing volume fractions of $(RGRGG)_5$–dT_{40} condensates. **(G)** Schematic of analytical HPLC assay to determine the dilute phase concentration (c_{dilute}) of A1-LCD in samples of protein–nucleic acid condensates. **(H)** c_{dilute} of WT A1-LCD in samples containing $(RGRGG)_5$–dT_{40} condensates at two different volume fractions. The data is represented as mean ± SEM, and the points indicate individual measurements. **(I)** Confocal fluorescence images of $(RGRGG)_5$–dT_{40} condensates either with or without A1-LCD D262V [visualized with 250 nM Alexa594-$(RGRGG)_5$] at the indicated time points after sample preparation. ThT was used to visualize amyloid fibrils. **(J)** 3D confocal Z-stack render of ThT-stained A1-LCD D262V fibrils and Cy5-dT_{40}–labeled $(RGRGG)_5$–dT_{40} condensates, imaged 8 hours after sample preparation. **(K)** Individual Z-slices corresponding to (J) are shown in the order of the bottom Z-slice to the top Z-slice, positioned from left to right. Also, see **Video S1**.

Condensates with higher viscoelasticity dampen fibril formation kinetics more effectively

Next, we sought to decipher which physical characteristics of condensates dampen fibril formation kinetics. Recent reports show that single and multi-component biomolecular condensates that form via phase separation coupled to percolation are network fluids with sequence-encoded viscoelastic material properties (*26, 33, 39, 40*). An appealing feature of the synthetic peptide–ssDNA condensates is their programmable viscoelasticity (*32, 41*). Subtly altering the sequence of the $(RGRGG)_5$ polypeptide while keeping the ssDNA component fixed tunes condensate viscoelasticity over three orders of magnitude (*32*). Substituting arginine with lysine or proline residues attenuates condensate viscoelasticity. Conversely, substituting the second arginine with a tyrosine residue strengthens condensate viscoelasticity. Furthermore, substituting glycine with proline as spacer residues weakens condensate viscoelasticity. First, to directly determine the frequency-dependent linear viscoelasticity of the three-component peptide–ssDNA–A1-LCD condensates, we used passive microrheology with optical tweezers (pMOT) (**Fig. 2A**), a technique we recently developed (*32*). The rank order of viscoelasticity, determined by frequency-dependent storage (G') and loss (G") moduli and their crossover frequency, showed a similar trend as the two-component peptide–ssDNA systems we previously reported (*32, 33*) (**Fig. 2B, C**). Specifically, condensates formed with RGPGG- and KGKGG-repeat peptides were the least viscoelastic, followed by those with RPRPP- and RGRGG-repeat peptides, while RGYGG-repeat peptides formed the most viscoelastic condensates with ssDNA (**Table S4**). This trend was quantified by (i) a progressive decrease in crossover frequency, ordered as $(KGKGG)_5$ > $(RGPGG)_5$ > $(RPRPP)_5$ > $(RGRGG)_5$ > $(RGYGG)_5$, and (ii) a monotonic increase in G' and G" at 1.0 Hz, ordered as $(KGKGG)_5$ < $(RGPGG)_5$ < $(RPRPP)_5$ < $(RGRGG)_5$ < $(RGYGG)_5$. Interestingly, we note that the viscosities of the three-component condensates were consistently higher than those of the two-component peptide–ssDNA systems (**Table S5**).

Next, we assessed the ability of these peptide–ssDNA–A1-LCD condensates to suppress fibril formation of WT A1-LCD (**Fig. S2A-C**) and the pathogenic D262V mutant (**Fig. 2D, Fig.**

S2D). For each type of condensate, increasing peptide and ssDNA concentrations progressively increased lag times on a system-specific timescale (**Fig. S2B, Fig. S2D**). Notably, at a fixed peptide–ssDNA concentration, condensates with higher viscoelasticity led to longer lag times (**Fig. 2D, E**). The lag time for fibril formation of the pathogenic mutant D262V in the presence of highly viscoelastic $(RGYGG)_5$–dT_{40} condensates (viscosity, η, 95.39 ± 5.17 Pa.s; terminal relaxation timescale, τ_M, at which G'/G" = 1, is 1086.87 ± 76.67 ms) is ~4 times longer relative to that of the least viscoelastic condensates, $(KGKGG)_5$–dT_{40} (η = 2.39 ± 0.43 Pa.s; τ_M = 25.87 ± 2.73 ms) (**Fig. 2E**). Similarly, increasing the viscoelasticity of peptide–ssDNA condensates resulted in progressive dampening of WT A1-LCD fibril formation (**Fig. S2C**).

SGs sequester untranslated RNA and are therefore classified as RNP granules (*4*). Therefore, we next assessed whether condensates formed by repeat peptides and rU_{40} RNA, in place of ssDNA, can similarly suppress fibril formation. Indeed, analogous to the samples containing peptide–ssDNA condensates, the lag times for fibril formation increased with increasing peptide–RNA concentrations (**Fig. 2F, Fig. S2E-F, Fig. S3A**). At a fixed peptide–RNA concentration, increasing condensate viscoelasticity similarly dampened fibril formation kinetics of the pathogenic D262V mutant (**Fig. 2F, Fig. S2E-F, Fig. S3A**). A range of simple RNP granule mimics can therefore robustly suppress fibril formation of A1-LCD. Overall, these results reveal a direct link between the sequence-encoded viscoelastic properties of heterotypic peptide–nucleic acid condensates and their ability to suppress fibril formation of partitioning A1-LCD molecules.

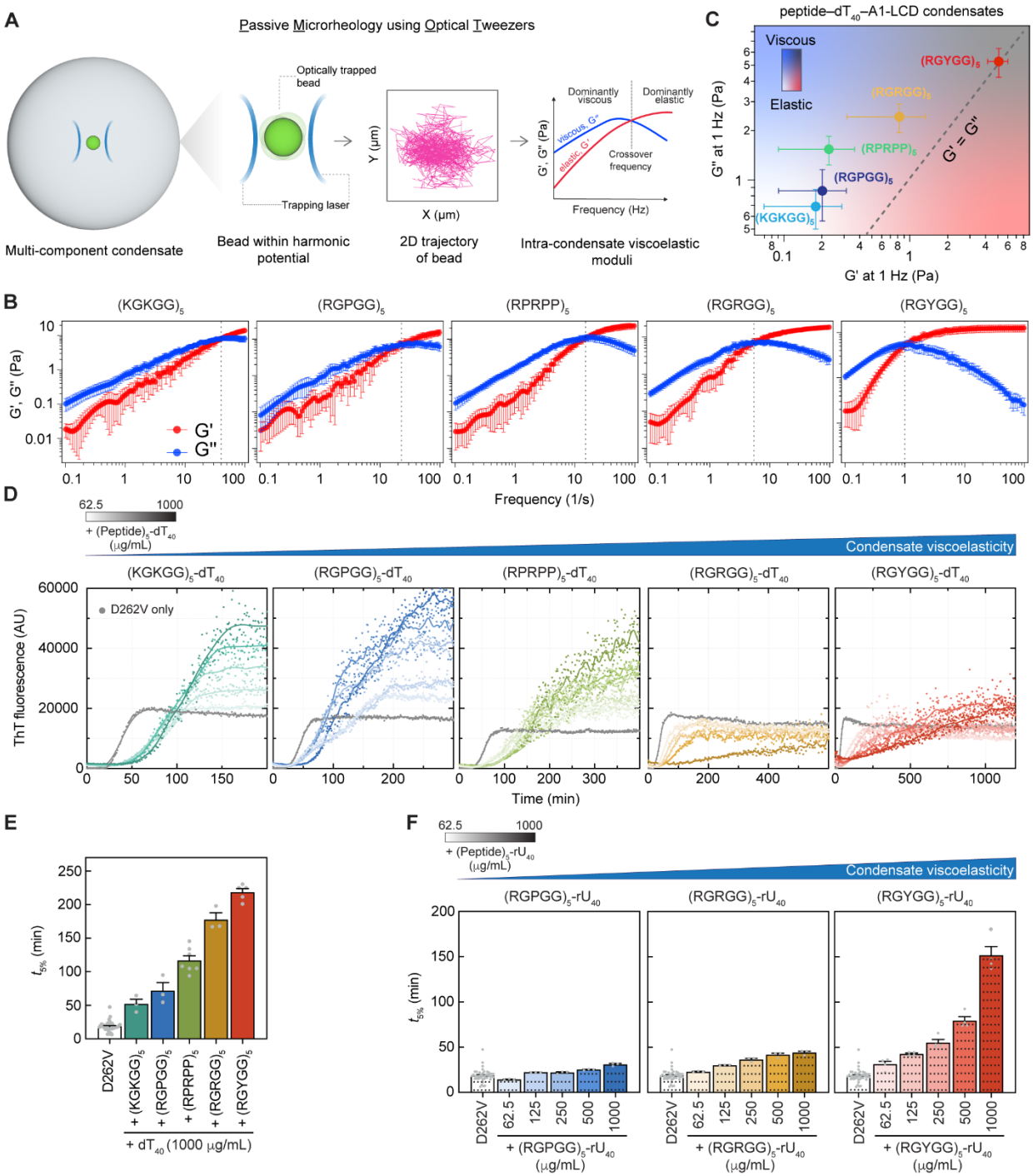

Figure 2. Higher viscoelasticity of multi-component biomolecular condensates prolongs lag times for fibril formation. (A) Schematic of passive microrheology using optical tweezers (pMOT) assay for measuring frequency-dependent viscous and elastic moduli of condensates. **(B)** Dynamical moduli for repeat peptide–nucleic acid condensates containing WT A1-LCD, wherein only the identity of the peptide component is varied, from pMOT measurements. G′ and G″ are the frequency-dependent storage and loss moduli, respectively. The data is represented as mean ± standard deviation (SD). The dashed line represents the crossover line. **(C)** Material state diagram of peptide–nucleic acid–WT A1-LCD condensates. The data is represented as mean ± SD. **(D)** Kinetics of fibril formation monitored by ThT fluorescence of 25 μM A1-LCD D262V either alone or in the presence of different multi-component condensate systems with

distinct viscoelasticity at a range of volume fractions, arranged in order of increasing condensate viscoelasticity from left to right. A smoothing window of 10 data points was applied to generate a connecting line. See the corresponding $t_{5\%}$ plots for all peptide–ssDNA concentrations tested in **Fig. S2D**. **(E)** Lag times ($t_{5\%}$) for the highest peptide–ssDNA concentrations extracted from the ThT kinetics shown in (D) and from replicate experiments ($n \geq 3$) are shown along with the mean ± SEM. **(F)** Lag times ($t_{5\%}$) extracted from the ThT kinetics in **Fig. S2E** of A1-LCD D262V either alone or in the presence of multi-component repeat peptide–RNA (i.e., rU_{40}) condensates. Lag times from replicate experiments ($n \geq 3$) are shown along with the mean ± SEM.

Protein dilute phase concentrations alone do not explain lag times with different peptide–ssDNA condensate systems

How do condensates with higher viscoelasticity more effectively suppress fibril formation? Given that fibrils grow in the dilute phase, and higher condensate volume fractions recruit more A1-LCD and slow down fibril formation more effectively, we hypothesized that the dilute phase concentrations (c_{dilute}) of A1-LCD determine nucleation and growth rates, and therefore the lag phase. Accordingly, condensates that suppress fibril formation more effectively should recruit more A1-LCD at a fixed peptide–ssDNA concentration, thereby lowering c_{dilute}. To test this, we determined c_{dilute} of A1-LCD in the presence of various condensates using analytical HPLC measurements (**Fig. 1G**) (*35*). At 62.5 μg/mL peptide and ssDNA, c_{dilute} of A1-LCD was between ~4 and 6 μM (**Fig. 3A**), whereas c_{dilute} was below 2 μM at 125 μg/mL peptide and ssDNA (**Fig. 3B**). At concentrations above 125 μg/mL peptide and ssDNA, c_{dilute} dropped below the detection limit of the HPLC-based measurements. Across all peptide–ssDNA condensates tested, increasing peptide and ssDNA concentrations progressively depleted A1-LCD from the dilute phase, as shown earlier for RGRGG-peptide–ssDNA condensates (**Fig. 1H**). Notably, c_{dilute} was highest for the RGRGG- and RGYGG-peptide–ssDNA condensates, which displayed the longest lag times. Conversely, samples with the lowest A1-LCD dilute phase concentrations, such as those with RGPGG-peptide–ssDNA condensates, in which the A1-LCD dilute phase concentration was too low to be measurable by analytical HPLC, showed the shortest lag times. Therefore, although dilute-phase concentration appears to be a key determinant of fibril growth for a given peptide–ssDNA condensate system as condensate volume fraction increases (**Fig. 1D, H**), it does not explain the differences in lag times observed across different peptide–ssDNA condensates with distinct viscoelastic properties.

We next determined the saturation concentration for fibril formation, c_{sf}, for WT A1-LCD in our buffer conditions, which was 0.3 μM (**Fig. 3A, B**). The dilute phase concentrations of A1-LCD were therefore below c_{sf} even at intermediate peptide–ssDNA concentrations for specific condensate systems. A1-LCD is not expected to form fibrils under these conditions. However, ThT bulk assays and ThT fluorescence microscopy suggested that fibrils do form under such conditions. To explain this conundrum, we performed nsTEM of sedimentable components in the samples after 6 days of incubation. While WT A1-LCD and the pathogenic mutant alone formed fibril bundles, we observed smaller, irregular assemblies in the presence of peptide–ssDNA condensates (**Fig. S4A**). These assemblies were observed to seed fibril formation, albeit to a relatively lesser extent than seeds generated from fibrils (**Fig. S4B-D,** see **Supplementary Note 1**). We conclude that these assemblies are likely early fibrils or pre-fibrillar species (**Fig. S4A**). We therefore interpret the ThT fluorescence signals from peptide–ssDNA–A1-LCD samples where the $c_{dilute} < c_{sf}$ to stem from nucleation of A1-LCD at interfaces followed by aborted fibril growth, given the low dilute phase concentrations of A1-LCD.

These collective observations prompt a mechanistic question: If the lag phase is not governed by the dilute phase A1-LCD concentration, which alternative factors determine fibril nucleation?

Protein density at condensate interfaces is a determinant of lag time

We and others recently demonstrated that interfaces of homotypic protein condensates promote fibril nucleation (*21-24, 38, 42, 43*). We therefore monitored the spatiotemporal distribution of ThT fluorescence over time in solutions containing $(RGRGG)_5$–dT_{40} condensates and the pathogenic D262V mutant using fluorescence microscopy. As early as two hours after sample preparation, ThT fluorescence increased at the interfaces of condensates, but not in the condensate interiors, suggesting that nucleation may also be promoted at the interfaces of multi-component condensates (**Fig. 3C, Video S2**). At later time points (≥ 8 hours), fluorescently labeled D262V molecules showed preferential accumulation at condensate interfaces, suggesting that interfacial fibril nucleation was followed by migration of protein molecules from the interior to the condensate interface (**Fig. S3B**). In condensates that were the least effective at lengthening lag times, including those formed with RGPGG-peptide, we observed migration of A1-LCD to the interface on a timescale of minutes (**Fig. 3D, Video S3**), as opposed to the timescale of hours required in samples with RGRGG-peptide (**Fig. S3B, Video S4**). Notably, after migration of protein from the condensate interior, a corona enriched in A1-LCD D262V remained (**Fig. 3E**). Fluorescence recovery after photobleaching (FRAP) measurements showed low fluorescence recovery of the D262V corona, suggesting that amyloid nucleation at the condensate interface results in the formation of a solid interfacial shell (**Fig. 3E**), reminiscent of observations of solid shells around FUS condensates (*23, 43*).

Given that condensate interfaces promote fibril nucleation, we wondered whether A1-LCD concentrations at interfaces, as opposed to concentrations in the dilute phase, are the factor determining nucleation rates. Using fluorescence microscopy, we determined the partition coefficients of labeled WT A1-LCD or D262V into peptide–ssDNA condensates (**Fig. S3C, D**). The fluorescence intensity of labeled A1-LCD remained homogeneously distributed throughout peptide–ssDNA condensates at early time points. We therefore used the relative partition coefficients of labeled WT and D262V A1-LCD as a proxy for A1-LCD concentrations at condensate interfaces. Strikingly, both A1-LCD variants partitioned more strongly into $(RGPGG)_5$–dT_{40} and $(KGKGG)_5$–dT_{40} condensates, i.e., those with the lowest viscoelasticity, compared to the more viscoelastic $(RGYGG)_5$–dT_{40} condensates. This differential partitioning can be mechanistically explained by competitive interactions between the A1-LCD and the repeat peptides for ssDNA binding (*see* **Supplementary Note 2**). Notably, condensates exhibiting higher WT A1-LCD partitioning also showed shorter fibril nucleation lag times, and vice versa (**Fig. 3F**). This inverse relationship between protein partitioning into condensates and lag time also held true for the D262V mutant (**Fig. 3G**). We note that the lag time is an empirical parameter that does not purely represent primary nucleation rate but also includes contributions from secondary nucleation and fibril growth rates. Overall, given that the interiors of condensates suppress fibril formation, our results suggest that protein concentrations at interfaces, so-called interface densities, of fibril-forming proteins play an important role in determining the timescale of fibril nucleation.

Based on these insights, we hypothesized that dilution of A1-LCD densities at condensate interfaces through competition with additional proteins may extend lag times and suppress fibril formation further. Given that SGs contain many different RBPs with PLDs, we tested the effect of adding a PLD variant that lacks the propensity to form fibrils but retains the ability to partition into peptide–ssDNA condensates (**Fig. S5**). We chose a variant of A1-LCD termed Δhexa, in which the primary steric zipper (^{259}SYNDFG^{264}), which includes the site of the disease mutation, is deleted (**Fig. 1A**) (*31*). When A1-LCD Δhexa was titrated into dilute solutions containing only A1-LCD D262V without peptide–ssDNA condensates, the kinetics of fibril formation remained unaffected (**Fig. 3H,** *left*). By contrast, the addition of increasing concentrations of A1-LCD Δhexa to solutions containing A1-LCD D262V, RGRGG-peptide, and dT_{40} progressively prolonged the

lag phase (**Fig. 3H**, *right*), although the partition coefficient of D262V in condensates did not change substantially (**Fig. S5**). These results support our conclusion that the relative density of fibril-forming protein at the condensate interface is one important determinant of fibril assembly lag phase (**Fig. 3H, I**), and this can therefore be lengthened considerably in multi-component condensates.

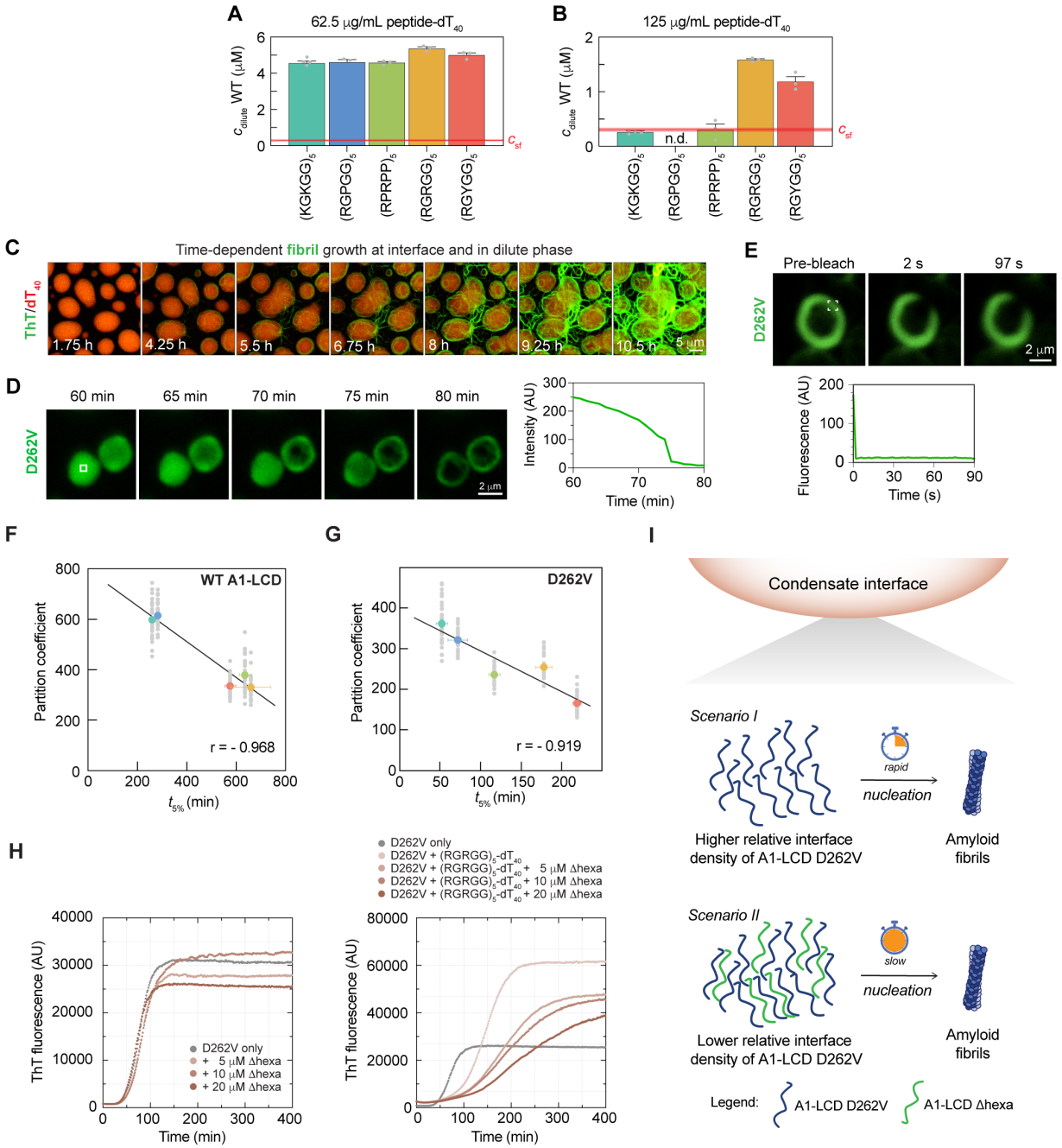

Figure 3. Higher interface densities of fibril-forming protein shorten lag times for fibril formation. (A, B) Dilute phase concentrations (c_{dilute}) of A1-LCD in samples of distinct multi-component condensate systems of varying viscoelastic properties at two different protein/nucleic acid concentrations of 62.5 μg/mL (A) or 125 μg/mL (B). In either plot, the data is represented as mean ± SEM, and the points indicate individual measurements. The c_{dilute} measurements of A1-LCD in samples containing $(RGRGG)_5$-dT_{40} condensates are reproduced from Fig. 1H. The saturation concentration for fibril formation (c_{sf}) of A1-LCD

is indicated as a red line with a shaded area, signifying the mean ± SEM. 'n.d.' here means "not determined". **(C)** Time-lapse maximum intensity projection images of $(RGRGG)_5$–dT_{40} condensates (visualized with 250 nM Cy5-dT_{40}) containing A1-LCD D262V. Fibrils were detected using ThT fluorescence (green). See also **Video S2**. **(D)** Time-lapse images to monitor the progressive loss of A1-LCD D262V (visualized with 250 nM Alexa488-D262V) from the interiors of $(RGPGG)_5$–dT_{40} condensates. The time-dependent fluorescence intensity change in the area of the white box is also shown. See also **Videos S3** and **S4**. **(E)** Fluorescence recovery after photobleaching (FRAP) profile of an A1-LCD corona (visualized using 250 nM Alexa488-D262V) from a $(KGKGG)_5$–dT_{40} condensate. This sample was imaged 1.5 hours after sample preparation. **(F, G)** Correlation analysis between partition coefficients of WT A1-LCD (F) and D262V (G) in different protein–nucleic acid condensates (as shown in **Fig. S3C, D**; individual measurements are shown along with the mean) versus the lag time ($t_{5\%}$ as shown in **Fig. 2E, Fig. S2C**; the mean is shown along with the SEM). A straight line shows the best fit for the correlation, and the Pearson correlation coefficient (r) is indicated. **(H)** Kinetics of fibril formation monitored by ThT fluorescence of 25 μM A1-LCD D262V either alone or with increasing concentrations of A1-LCD Δhexa, either in the absence (left) or presence (right) of $(RGRGG)_5$–dT_{40} condensates. A smoothing window of 10 data points was applied to generate a connecting line. **(I)** Schematic representing the observed effect of A1-LCD interface density on fibril formation, either in the absence or presence of A1-LCD Δhexa.

Condensates with higher viscoelasticity generated through longer nucleic acids decelerate fibril growth

Because the material properties of the condensates were tuned by using peptides with different chemical makeup (**Figs. 2 & 3**), the observed changes in A1-LCD fibril formation kinetics may be influenced by the peptide−A1-LCD interactions. We recently showed that increasing the length of the condensate-scaffolding nucleic acid while keeping the identity of the scaffolding peptide fixed is an alternative route to tuning condensate viscoelasticity (*33*). Therefore, we used this orthogonal approach to tune the viscoelasticity of multi-component condensates that precludes changes to the peptide molecular grammar. When we varied the poly-dT chain length from 20 to 200 nucleobases and combined these with the RGRGG-peptide, the viscosities of the resulting condensate systems spanned a ~17-fold range (**Fig. 4A**). We examined fibril formation of A1-LCD D262V in the presence of these heterotypic condensates of varying viscoelasticity. Analytical HPLC measurements revealed that the A1-LCD dilute phase concentrations were progressively lower for longer poly-dT ssDNA (**Fig. S6C**), but the partition coefficients of A1-LCD D262V into condensates formed with different ssDNA chain length were very similar to each other (**Fig. 4B**). However, samples with longer ssDNA with enhanced viscoelasticity resulted in longer lag times (**Fig. S6A, Fig. 4C**). Furthermore, time course microscopy images reveal a notable feature: Condensates with the longest ssDNA displayed CRANAD2-positive rims for many hours without obvious signs of microscopically detectable fibrils in the dilute phase, whereas fibrils were detected around condensates with shorter ssDNA within a few hours (**Fig. S6B**). These observations suggested that fibril nucleation had occurred, yet fibrils did not grow in the dilute phase of samples containing heterotypic condensates scaffolded by longer ssDNA. These observations are in accordance with our earlier observation that nucleation of A1-LCD occurs at condensate interfaces, but mature fibrils fail to grow if the dilute phase concentration is below c_{sf}, which is the case with more viscoelastic condensates. Notably, these data confirm that condensate viscoelasticity plays a key role in suppressing fibril formation in a manner independent of effects from A1-LCD partitioning.

High internal condensate network strength slows the efflux of fibril-forming protein

Why do condensates with higher viscoelasticity but similar A1-LCD partitioning increase the lag times more than condensates with lower viscoelasticity? We hypothesized that the efflux rates of

A1-LCD from peptide-ssDNA condensates into the dilute phase would differ across condensates of varying viscoelasticity and that limited efflux from highly viscoelastic condensates may reduce the availability of A1-LCD in the dilute phase, thereby slowing the growth of ThT-positive species. To directly track the kinetics of recruitment and retention of A1-LCD in peptide-ssDNA condensates of varying viscoelasticity, we developed a real-time quantitative assay that takes advantage of microfluidics, correlative confocal fluorescence microscopy and a dual trap laser tweezer system (**Fig. 4D**). Briefly, we optically trapped a single peptide–ssDNA condensate under laminar flow in one channel [Channel 1 (Ch1)] of a microfluidic chamber and moved it at a controlled velocity to an adjacent channel containing buffer only (Ch2), and eventually to a third adjoining channel (Ch3) containing fluorescently labeled A1-LCD D262V under laminar flow. Continuous fluorescence imaging allowed us to capture the kinetics of client recruitment to the optically trapped condensate while in Ch3. The condensate was kept in this channel for 100 s to measure the extent and speed of client recruitment. Subsequently, the condensate was moved back to the buffer channel (Ch2) to measure the extent and speed of client efflux (**Fig. 4D**).

We first tracked recruitment and retention of TMR-labeled dextran-4.4K, a non-specific client that favorably partitions into peptide-ssDNA condensates (**Fig. S6D**), in two condensates with different viscoelasticity. Recruitment of dextran-4.4K into $(RGRGG)_5$–dT_{40} (viscosity = 3.28 ± 0.06 Pa.s) and $(RGRGG)_5$–dT_{200} condensates (viscosity = 23.24 ± 1.24 Pa.s) plateaued by ~100 s (**Fig. 4A, E**). The recruitment kinetics into the dT_{40} condensate system with lower viscosity was somewhat faster than into the dT_{200} condensates with higher viscosity. Moving the condensate back to the buffer-only channel resulted in progressive efflux of dextran on similar timescales for both types of condensates (**Fig. 4F**). Hence, the efflux rates of dextran are not dependent on the bulk viscosity differences of condensates (**Fig. 4J**), indicating (a) the molecular size of dextran is lower than the correlation length or the average mesh size of the condensates (*44, 45*), and (b) the client does not engage in dominant interactions with the viscoelastic network of peptide-ssDNA condensates.

Next, we performed the recruitment and retention assay with Alexa488-labeled A1-LCD D262V. The recruitment of A1-LCD D262V into either condensate occurred on a similar timescale, although somewhat slower for the condensate with the higher viscoelasticity (**Fig. 4G-H, Videos S5, S6**). By contrast, the protein efflux from highly viscoelastic $(RGRGG)_5$–dT_{200} condensates was markedly slower than the efflux from less viscoelastic $(RGRGG)_5$–dT_{40} condensates (**Fig. 4G, I, Videos S5, S6**). The efflux time constants (τ) extracted from time-dependent fluorescence decay curves indicate that the more viscoelastic condensates retain A1-LCD D262V molecules for a significantly longer period (τ ~ 960 s) than the less viscoelastic condensates (τ ~ 428 s) (**Fig. 4J**). Hence, the difference in the strength of the underlying condensate-spanning network, which manifests as condensate viscoelasticity, is a key determinant of the A1-LCD efflux rate (**Fig. 4K**). Of note, the efflux assay performed here is an active measurement under flow; the difference in efflux rates could be even larger under steady-state conditions. Overall, these results suggest that multi-component condensates with higher viscoelastic network strength release fibril-forming proteins more slowly than the typical rate of protein incorporation into fibrils in the dilute phase, creating a kinetic bottleneck in fibril assembly and dictating the duration of the lag phase and therefore the overall kinetics of fibril assembly.

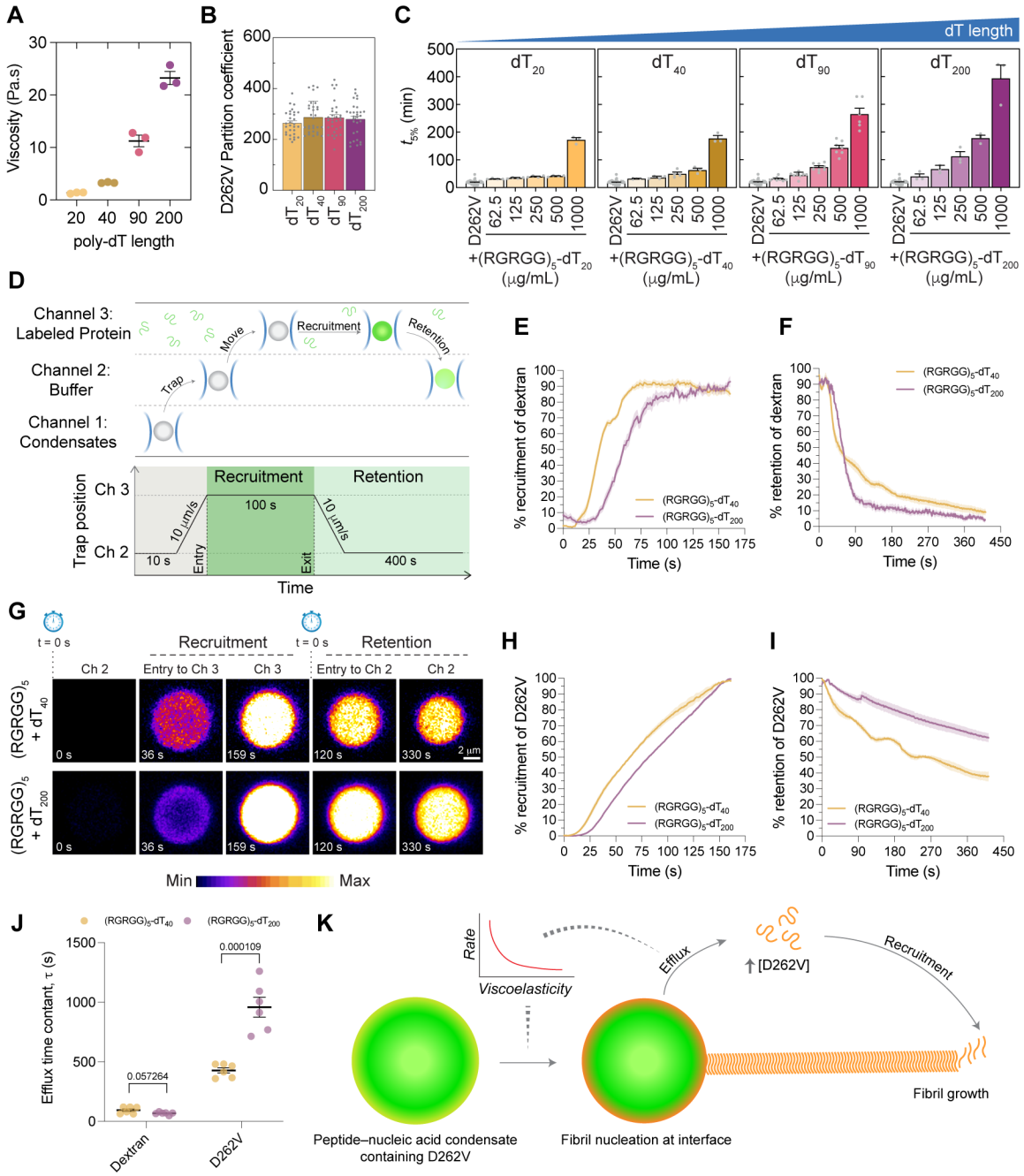

Figure 4. Enhanced condensate viscoelasticity slows down the efflux of fibril-forming protein and limits fibril growth. (A) Video particle tracking (VPT) nanorheology-based viscosities of peptide–ssDNA condensates [$(RGRGG)_5$ and poly-dT of increasing chain length)] at fixed concentrations of 5 mg/mL peptide and nucleic acid. The points indicate data from three independent replicates, and are shown along with mean ± SEM. Raw data from Alshareedah et al. 2024 was reproduced to generate this plot (*33*). **(B)** Partition coefficients of Alexa488-labeled D262V in peptide–ssDNA condensates [$(RGRGG)_5$ and poly-dT of increasing chain length] at fixed concentrations of 1 mg/mL peptide and nucleic acid. The points represent individual measurements from three independent replicates and are reported along with mean ± SD. **(C)** Lag times ($t_{5\%}$) extracted from ThT kinetics (see **Fig. S6A**) monitoring D262V fibril formation either in the absence or presence of increasing concentrations of $(RGRGG)_5$ and poly-dT ssDNA of distinct chain lengths. Data from replicate experiments ($n \geq 3$) are shown along with the mean ± SEM. **(D)** (top) Schematic

depicting the principle of the condensate recruitment and retention assay involving the simultaneous use of microfluidics, optical trapping, and fluorescence microscopy to determine the influx and efflux kinetics of fluorescently labeled client molecules into and out of multi-component condensates. (bottom) Schematic of the trajectory followed by the optical trap in the microfluidic chamber across different channels (Ch). **(E)** Recruitment kinetics of TMR-labeled dextran-4.4K into $(RGRGG)_5$–dT_{40} and $(RGRGG)_5$–dT_{200} condensates reported as mean ± SEM. **(F)** Retention kinetics of TMR-labeled dextran-4.4K in $(RGRGG)_5$–dT_{40} and $(RGRGG)_5$–dT_{200} condensates reported as mean ± SEM. **(G)** Time-lapse fluorescence images of Alexa488-labeled D262V showing partitioning at different stages of the recruitment and retention assay, in $(RGRGG)_5$–dT_{40} and $(RGRGG)_5$–dT_{200} condensates. Also see **Videos S5** and **S6**. The displayed maximum intensity threshold value of the image panels of $(RGRGG)_5$–dT_{40} and $(RGRGG)_5$–dT_{200} was adjusted independently for optimal visualization. **(H)** Recruitment kinetics of Alexa488-labeled D262V into $(RGRGG)_5$–dT_{40} and $(RGRGG)_5$–dT_{200} condensates reported as mean ± SEM. **(I)** Retention kinetics of Alexa488-labeled D262V in $(RGRGG)_5$–dT_{40} and $(RGRGG)_5$–dT_{200} condensates reported as mean ± SEM. **(J)** Efflux time constants of either dextran-4.4K or D262V in $(RGRGG)_5$–dT_{40} and $(RGRGG)_5$–dT_{200} condensates, extracted from the corresponding retention kinetics by fitting to a stretched exponential decay. Statistical significance was determined by performing unpaired *t*-tests between the highlighted pairs of data, with the estimated p-value displayed above. The points indicate individual measurements from three independent replicates and are shown along with mean ± SEM. **(K)** Schematic highlighting the impact of condensate viscoelasticity in determining the rate of efflux of fibril-forming protein from condensate interiors, serving as a rate-limiting step in fibril growth.

G3BP1–RNA condensates protect against A1-LCD fibril formation

Our observations so far suggest three key features by which multi-component peptide–nucleic acid condensates regulate fibril formation: (1) Given that fibrils form in the dilute phase, strong partitioning of the fibril-forming protein into condensates lowers its concentration in the dilute phase and slows down or even abrogates fibril growth. (2) Lower effective densities of the fibril-forming protein at the interfaces of multi-component condensates reduce nucleation and lengthen lag times. (3) Higher condensate viscoelasticity reduces the efflux of fibril-forming proteins into the dilute phase and limits fibril growth. To what extent are these observations generalizable to biologically relevant SG mimics?

Given that G3BP and poly-A tail–containing mRNA are essential for SG assembly and form the core network that recruits other RBPs (*2*), we tested whether multi-component condensates consisting of G3BP1, poly-rA, and A1-LCD could similarly suppress A1-LCD fibril formation (**Fig. 5A**). Using fluorescence microscopy, we first confirmed that A1-LCD D262V strongly partitions into G3BP1–poly-rA condensates (**Fig. 5B**). We then used ThT fluorescence to monitor A1-LCD D262V fibril formation both alone and in the presence of increasing concentrations of G3BP1 and poly-rA at a constant ratio. Higher concentrations of condensate-forming components indeed led to progressively longer lag times (**Fig. 5C**, **Fig. S7A**). Notably, we observed enhanced fluorescence intensity of the amyloid dye CRANAD2 at condensate interfaces, consistent with the interpretation that fibril nucleation occurs at the interfaces of condensates. This is followed by redistribution of A1-LCD from the condensate interior to the interface and accumulation of A1-LCD fibrils in the dilute phase over time (**Fig. 5D, E**). To probe whether reduced interface density can mitigate fibril nucleation, we titrated increasing concentrations of the A1-LCD Δhexa variant into D262V–G3BP1–poly-rA mixtures and found a progressive delay in fibril formation (**Fig. 5F**). Consistent with our findings in peptide–nucleic acid condensates, we did not observe typical fibrils in the presence of G3BP1–poly-rA condensates but rather, small, irregular assemblies that may be accumulated nuclei or protofibrils (**Fig. S7B**).

Collectively, these findings demonstrate that *in vitro* SG facsimiles can suppress A1-LCD fibril formation, and that the physical principles, such as interface-mediated nucleation and sequestration of soluble protein in the interior of condensates, govern fibril kinetics in multi-

component systems, including physiological SG components (**Fig. 5G**).

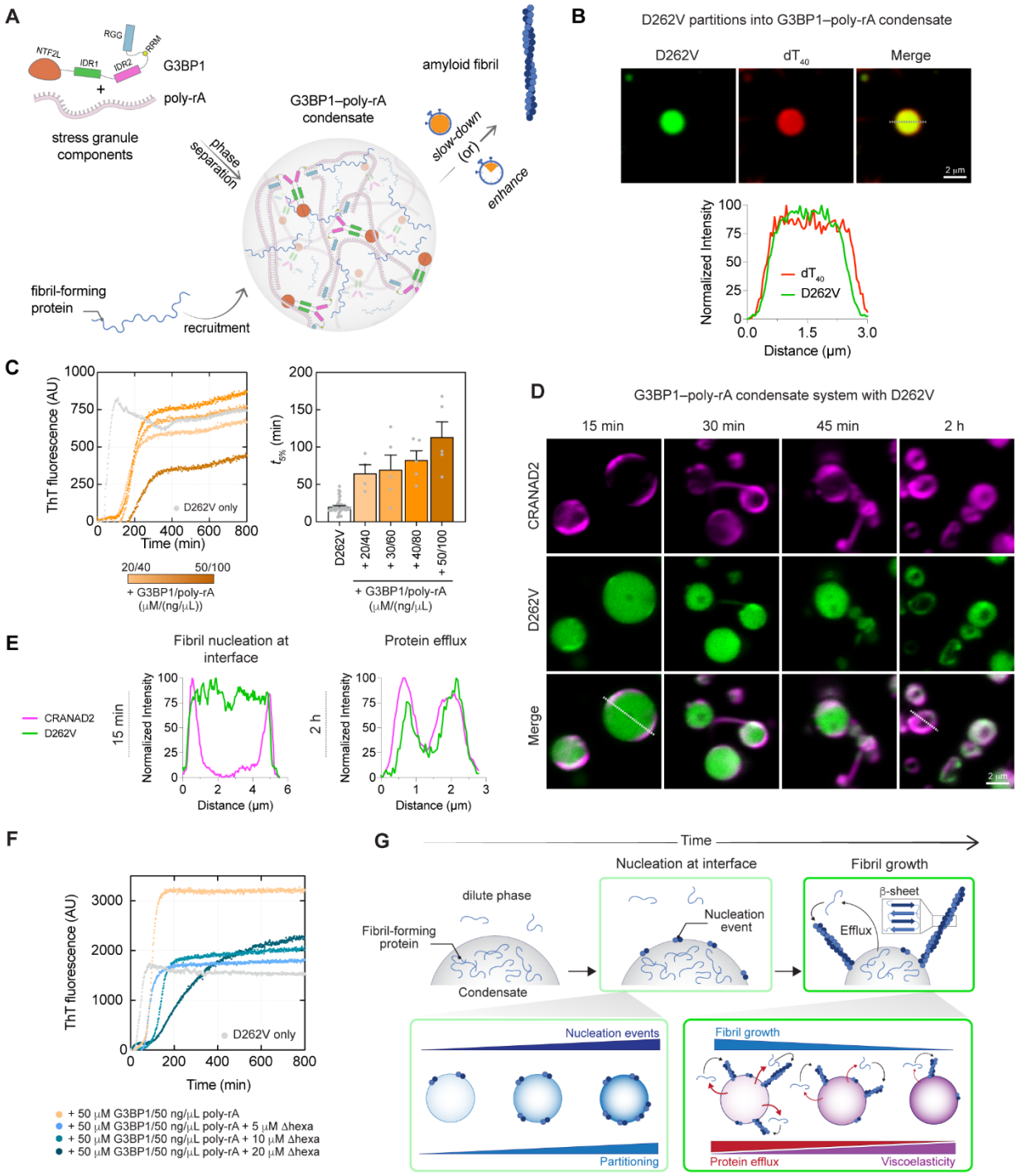

Figure 5. G3BP1–RNA condensates suppress A1-LCD fibril formation. (A) Schematic illustrating the experimental system to test whether condensates formed by primary SG components, G3BP1 and poly-rA, either promote or suppress amyloid fibril formation of A1-LCD. **(B)** Fluorescence images showing favorable partitioning of D262V (visualized with 250 nM Alexa488-D262V) into G3BP1–poly-rA condensates (visualized with 250 nM of anti-sense Cy5-dT_{40}). The corresponding line profiles are shown. **(C)** (left)

Kinetics of fibril formation monitored by ThT fluorescence of 25 μM A1-LCD D262V either alone or in the presence of G3BP1–poly-rA condensates at a range of volume fractions. Baseline subtraction was applied, and a smoothing window of 10 data points was used to generate a connecting line. (right) Lag times ($t_{5\%}$) extracted from ThT kinetics (shown on the *left*) and replicate experiments ($n \geq 3$) are shown along with the mean ± SEM. **(D)** Fluorescence image time course of G3BP1–poly-rA condensates with D262V (visualized with 250 nM Alexa488-D262V) showing CRANAD2 fluorescence at the interfaces and fibrillar structures appearing in the dilute phase (visualized with CRANAD2), supported by corresponding line profile analyses, shown in **(E)**. Images in panel (D) were adjusted independently for optimal visualization of the coexistence of droplets and fibrils in each condition. **(F)** Kinetics of fibril formation monitored by ThT fluorescence of 25 μM A1-LCD D262V alone, in the presence of G3BP1–poly-rA condensates, and with increasing concentrations of A1-LCD Δhexa in the presence of G3BP1–poly-rA condensates. Baseline subtraction was applied, and a smoothing window of 10 data points was used. **(G)** Schematic summarizing the main findings of this study, highlighting three key roles of condensates: sequestration of fibril-forming proteins, regulation of fibril nucleation through interface density, and control of protein efflux, and thus fibril growth, in the dilute phase via condensate viscoelasticity.

Interface density and viscoelasticity of heterotypic condensates determine their ability to suppress fibril formation

Through quantitative and systematic measurements and the use of model heterotypic peptide–nucleic acid condensates with physicochemical tunability, our experiments provide direct mechanistic insights into the influence of multi-component SG mimics on the fibril formation of the disease-relevant prion-like A1-LCD (**Fig. 5G**): (1) Fibrils grow in the dilute phase. Therefore, sequestration of fibril-forming protein in condensates suppresses fibril assembly. Suitable multi-component condensates can lower the dilute phase concentration of fibril-forming proteins below c_{sf}, which renders condensates the stable species and eliminates fibril growth. (2) Condensate interfaces contribute to fibril nucleation. Dilution of fibril-forming protein at interfaces in multi-component condensates lengthens lag times and therefore strongly delays fibril formation. (3) The efflux rate from condensates determines the concentration of protein that is available for fibril growth in the dilute phase. (4) Highly viscoelastic, internally percolated condensates slow down protein efflux and therefore suppress fibril growth. Importantly, these detailed insights gained from mechanistic interrogation of the tunable repeat peptide–nucleic acid condensates are generalizable to more complex and physiologically-relevant G3BP1–poly-rA SG mimics.

Our results show decisive advantages of multi-component condensates, highlighting their emergent property to suppress fibril formation. Homotypic condensates are metastable phases compared to fibrils and can serve as kinetic sinks for soluble protein (*21*). By contrast, if the dilute phase concentration of the fibril-forming protein is lower than c_{sf}, multi-component condensates are the thermodynamically stable state, in which case they become naturally protective. They also offer additional degrees of freedom. In mono-component condensates, enhanced metastability and the resultant high sink potential are inherently coupled to a high density of the fibril-forming protein at interfaces, which in turn promotes nucleation, generating a duality of interface and interior. Multi-component condensates enable decoupling of these properties: Condensates with highly viscoelastic internal network but relatively lower A1-LCD densities at interfaces are most effective at suppressing fibril formation. Importantly, the ability of multi-component condensates to suppress amyloid assembly cannot be explained by the behavior of individual condensate-forming components, underscoring their emergent properties (**Supplementary Note 3; Fig. S8**).

Our work suggests that RNP granules optimally suppress pathological fibril assembly if they (a) lower the dilute phase concentration of fibril-forming protein below c_{sf}, (b) dilute the relative density of fibril-forming protein at interfaces by recruiting multiple proteins through favorable homotypic and heterotypic interactions, and (c) engage in strong networking

interactions with the fibril-forming protein within the condensate microenvironment to control the rate of protein efflux. We posit that the multi-component nature of SGs achieves these properties and promotes heterotypic buffering, a previously proposed concept (*25, 46*), through thermodynamic frustration (*47, 48*). In support of point (c), our previous experiments aimed at enhancing the strength of the PLD network in intracellular SGs by mutagenesis successfully rescued delayed SG disassembly, a typical phenotype promoted by the expression of disease-causing RBP mutants, and restored normal SG disassembly (*21*).

We posit that the interior of homotypic condensates can suppress fibril formation because condensate and fibril formation often involve overlapping sequence determinants in fibril-forming proteins, creating competing interactions that can hinder the progression of fibril assembly (*21, 38*). However, we expect that not all condensates will suppress fibril formation of all fibril-forming proteins, because the extent of suppression will depend on the specific overlap between the sequence features that drive condensate formation and those that promote fibril assembly. For example, polymerization reactions such as actin polymerization can be promoted at condensate sites (*49*). By contrast, multi-component condensates may have additional degrees of freedom to suppress amyloid fibril formation if they effectively engage in heterotypic interactions with amyloidogenic segments and frustrate their homotypic interactions. Therefore, condensates may be permissive, or even facilitative, of fibril formation if the fibril-forming sequence features are not engaged in the condensate network. This nuanced view is supported by the observation that condensates formed by the intrinsically disordered region of CAPRIN1 suppress fibril formation of the RRM domain of FUS but promote fibril formation of SOD1, although the CAPRIN1 condensates destabilize the folded state of both proteins (*50, 51*).

The fact that phase separation and fibril formation are both highly concentration-dependent processes that are mediated by overlapping sequence features in the same protein results in the potential for misinterpretations of data that assess fewer dimensions of the process. As an example, purely light-microscopic observations are blind to the processes occurring in the dilute phase. Our mechanistic insights required a combination of quantitative thermodynamic and kinetic measurements over a range of protein concentrations and careful testing of alternative hypotheses.

In summary, our findings suggest that SGs and other RNP condensates do not typically promote protein fibril formation, which is in contrast to the prevalent view (*52-54*). We therefore propose that they do not serve as crucibles for protein aggregation and numerous neurodegenerative disorders (*12*). Further research will test the hypothesis that the stabilization of SG interiors can rescue key pathogenic processes driven by fibril formation of RBPs.

References

1. S. Hofmann, N. Kedersha, P. Anderson, P. Ivanov, Molecular mechanisms of stress granule assembly and disassembly. *Biochim Biophys Acta Mol Cell Res* **1868**, 118876 (2021).

2. P. Yang *et al.*, G3BP1 Is a Tunable Switch that Triggers Phase Separation to Assemble Stress Granules. *Cell* **181**, 325-345.e328 (2020).

3. D. W. Sanders *et al.*, Competing Protein-RNA Interaction Networks Control Multiphase Intracellular Organization. *Cell* **181**, 306-324.e328 (2020).

4. D. S. W. Protter, R. Parker, Principles and Properties of Stress Granules. *Trends Cell Biol* **26**, 668-679 (2016).

5. P. Anderson, N. Kedersha, Stress granules: the Tao of RNA triage. *Trends in Biochemical Sciences* **33**, 141-150 (2008).

6. J. Guillen-Boixet *et al.*, RNA-Induced Conformational Switching and Clustering of G3BP Drive Stress Granule Assembly by Condensation. *Cell* **181**, 346-361 e317 (2020).

7. B. Wolozin, P. Ivanov, Stress granules and neurodegeneration. *Nature Reviews Neuroscience* **20**, 649-666 (2019).

8. P. Zhang *et al.*, Chronic optogenetic induction of stress granules is cytotoxic and reveals the evolution of ALS-FTD pathology. *eLife* **8**, e39578 (2019).

9. J. P. Taylor, Multisystem proteinopathy: intersecting genetics in muscle, bone, and brain degeneration. *Neurology* **85**, 658-660 (2015).

10. I. R. Mackenzie *et al.*, TIA1 Mutations in Amyotrophic Lateral Sclerosis and Frontotemporal Dementia Promote Phase Separation and Alter Stress Granule Dynamics. *Neuron* **95**, 808-816.e809 (2017).

11. N. B. Nedelsky, J. P. Taylor, Pathological phase transitions in ALS-FTD impair dynamic RNA-protein granules. *RNA* **28**, 97-113 (2022).

12. Y. R. Li, O. D. King, J. Shorter, A. D. Gitler, Stress granules as crucibles of ALS pathogenesis. *Journal of Cell Biology* **201**, 361-372 (2013).

13. Q. Cui, Z. Liu, G. Bai, Friend or foe: The role of stress granule in neurodegenerative disease. *Neuron* **112**, 2464-2485 (2024).

14. Y. Lin, D. S. Protter, M. K. Rosen, R. Parker, Formation and Maturation of Phase-Separated Liquid Droplets by RNA-Binding Proteins. *Mol Cell* **60**, 208-219 (2015).

15. A. Patel *et al.*, A Liquid-to-Solid Phase Transition of the ALS Protein FUS Accelerated by Disease Mutation. *Cell* **162**, 1066–1077 (2015).

16. A. Molliex *et al.*, Phase separation by low complexity domains promotes stress granule assembly and drives pathological fibrillization. *Cell* **163**, 123-133 (2015).

17. S. Lu *et al.*, Heat-shock chaperone HSPB1 regulates cytoplasmic TDP-43 phase separation and liquid-to-gel transition. *Nat Cell Biol* **24**, 1378-1393 (2022).

18. F. Gasset-Rosa *et al.*, Cytoplasmic TDP-43 De-mixing Independent of Stress Granules Drives Inhibition of Nuclear Import, Loss of Nuclear TDP-43, and Cell Death. *Neuron* **102**, 339-357.e337 (2019).

19. J. R. Mann *et al.*, RNA Binding Antagonizes Neurotoxic Phase Transitions of TDP-43. *Neuron* **102**, 321-338.e328 (2019).

20. A. Dubinski *et al.*, Stress granule assembly in vivo is deficient in the CNS of mutant TDP-43 ALS mice. *Human Molecular Genetics* **32**, 319-332 (2022).

21. T. Das *et al.*, Tunable metastability of condensates reconciles their dual roles in amyloid fibril formation. *Molecular Cell* **85**, 2230-2245.e2237 (2025).

22. W. P. Lipiński *et al.*, Biomolecular condensates can both accelerate and suppress aggregation of α-synuclein. *Science Advances* **8**, eabq6495 (2022).

23. Y. Shen *et al.*, The liquid-to-solid transition of FUS is promoted by the condensate surface. *Proc Natl Acad Sci U S A* **120**, e2301366120 (2023).

24. M. Linsenmeier *et al.*, The interface of condensates of the hnRNPA1 low-complexity domain promotes formation of amyloid fibrils. *Nat Chem* **15**, 1340-1349 (2023).

25. C. Mathieu, R. V. Pappu, J. P. Taylor, Beyond aggregation: Pathological phase transitions in neurodegenerative disease. *Science* **370**, 56-60 (2020).

26. I. Alshareedah *et al.*, Sequence-specific interactions determine viscoelasticity and ageing dynamics of protein condensates. *Nature Physics* **20**, 1482-1491 (2024).

27. T. Mittag, R. Parker, Multiple Modes of Protein-Protein Interactions Promote RNP Granule Assembly. *J Mol Biol* **430**, 4636-4649 (2018).

28. J. Y. Youn *et al.*, Properties of Stress Granule and P-Body Proteomes. *Mol Cell* **76**, 286-294 (2019).

29. D. S. W. Protter *et al.*, Intrinsically Disordered Regions Can Contribute Promiscuous Interactions to RNP Granule Assembly. *Cell Rep* **22**, 1401-1412 (2018).

30. N. L. Gotor *et al.*, RNA-binding and prion domains: the Yin and Yang of phase separation. *Nucleic Acids Res* **48**, 9491-9504 (2020).

31. H. J. Kim *et al.*, Mutations in prion-like domains in hnRNPA2B1 and hnRNPA1 cause multisystem proteinopathy and ALS. *Nature* **495**, 467-473 (2013).

32. I. Alshareedah, M. M. Moosa, M. Pham, D. A. Potoyan, P. R. Banerjee, Programmable viscoelasticity in protein-RNA condensates with disordered sticker-spacer polypeptides. *Nat. Commun.* **12**, 1–14 (2021).

33. I. Alshareedah *et al.*, Determinants of viscoelasticity and flow activation energy in biomolecular condensates. *Science Advances* **10**, eadi6539 (2024).

34. H. Naiki, K. Higuchi, M. Hosokawa, T. Takeda, Fluorometric determination of amyloid fibrils in vitro using the fluorescent dye, thioflavin T1. *Anal Biochem* **177**, 244-249 (1989).

35. A. Bremer *et al.*, Quantifying Coexistence Concentrations in Multi-Component Phase-Separating Systems Using Analytical HPLC. *Biomolecules* **12**, (2022).

36. X. Yan *et al.*, Intra-condensate demixing of TDP-43 inside stress granules generates pathological aggregates. *Cell* **188**, 4123-4140.e4118 (2025).

37. D. Dormann, E. A. Lemke, Adding intrinsically disordered proteins to biological ageing clocks. *Nature Cell Biology* **26**, 851-858 (2024).

38. T. S. Mahendran *et al.*, Decoupling Phase Separation and Fibrillization Preserves Activity of Biomolecular Condensates. *bioRxiv*, 2025.2003.2018.643977 (2025).

39. H. H. Cheng *et al.*, Micropipette aspiration reveals differential RNA-dependent viscoelasticity of nucleolar subcompartments. *Proceedings of the National Academy of Sciences* **122**, e2407423122 (2025).

40. J. A. Riback *et al.*, Viscoelasticity and advective flow of RNA underlies nucleolar form and function. *Mol Cell* **83**, 3095-3107.e3099 (2023).

41. E. W. Martin *et al.*, Valence and patterning of aromatic residues determine the phase behavior of prion-like domains. *Science* **367**, 694–699 (2020).

42. C. H. Choi, D. S. W. Lee, D. W. Sanders, C. P. Brangwynne, Condensate interfaces can accelerate protein aggregation. *Biophys J* **123**, 1404-1413 (2024).

43. L. Emmanouilidis *et al.*, A solid beta-sheet structure is formed at the surface of FUS droplets during aging. *Nat Chem Biol* **20**, 1044-1052 (2024).

44. N. Galvanetto *et al.*, Extreme dynamics in a biomolecular condensate. *Nature* **619**, 876-883 (2023).

45. M.-T. Wei *et al.*, Phase behaviour of disordered proteins underlying low density and high permeability of liquid organelles. *Nature Chemistry* **9**, 1118-1125 (2017).

46. T. S. Mahendran, G. M. Wadsworth, A. Singh, R. Gupta, P. R. Banerjee, Homotypic RNA clustering accompanies a liquid-to-solid transition inside the core of multi-component biomolecular condensates. *Nature Chemistry* **17**, 1236-1246 (2025).

47. D. U. Ferreiro, E. A. Komives, P. G. Wolynes, Frustration in biomolecules. *Q Rev Biophys* **47**, 285-363 (2014).

48. D. U. Ferreiro, E. A. Komives, P. G. Wolynes, Frustration, function and folding. *Current Opinion in Structural Biology* **48**, 68-73 (2018).

49. K. Graham *et al.*, Liquid-like VASP condensates drive actin polymerization and dynamic bundling. *Nature Physics*, (2023).

50. R. Ahmed *et al.*, Atomic resolution map of the solvent interactions driving SOD1 unfolding in CAPRIN1 condensates. *Proceedings of the National Academy of Sciences* **121**, e2408554121 (2024).

51. R. Ahmed, R. P. Hudson, J. D. Forman-Kay, L. E. Kay, Client-scaffold interactions suppress aggregation of a client protein in model condensates. *bioRxiv*, 2025.2004.2011.648422 (2025).

52. B. S. Visser, W. P. Lipiński, E. Spruijt, The role of biomolecular condensates in protein aggregation. *Nature Reviews Chemistry* **8**, 686-700 (2024).

53. S. Alberti, A. A. Hyman, Biomolecular condensates at the nexus of cellular stress, protein aggregation disease and ageing. *Nat. Rev. Mol. Cell Biol.* **22**, 196–213 (2021).

54. M. Vendruscolo, M. Fuxreiter, Sequence Determinants of the Aggregation of Proteins Within Condensates Generated by Liquid-liquid Phase Separation. *J. Mol. Biol.* **434**, 167201 (2022).

55. A. Bremer *et al.*, Deciphering how naturally occurring sequence features impact the phase behaviours of disordered prion-like domains. *Nat Chem* **14**, 196-207 (2022).

56. I. Alshareedah *et al.*, Interplay between Short-Range Attraction and Long-Range Repulsion Controls Reentrant Liquid Condensation of Ribonucleoprotein-RNA Complexes. *J Am Chem Soc* **141**, 14593-14602 (2019).

57. J. Schindelin *et al.*, Fiji: an open-source platform for biological-image analysis. *Nature methods* **9**, 676-682 (2012).

58. M. Tassieri, R. M. L. Evans, R. L. Warren, N. J. Bailey, J. M. Cooper, Microrheology with optical tweezers: data analysis. *New Journal of Physics* **14**, 115032 (2012).

59. T. G. Mason, D. A. Weitz, Optical Measurements of Frequency-Dependent Linear Viscoelastic Moduli of Complex Fluids. *Physical Review Letters* **74**, 1250-1253 (1995).

60. K. C. Neuman, S. M. Block, Optical trapping. *Review of Scientific Instruments* **75**, 2787-2809 (2004).

61. J.-Y. Tinevez *et al.*, TrackMate: An open and extensible platform for single-particle tracking. *Methods (San Diego, Calif.)* **115**, 80-90 (2017).

Acknowledgments: We thank Drs. Rohit Pappu (Washington University in St. Louis) and Kresten Lindorff-Larsen (University of Copenhagen) for valuable discussions at various stages of the manuscript preparation.

Funding:

National Institutes of Health grant R01NS121114 (TM)
National Institutes of Health grant R35 GM138186 (PRB)
St. Jude Children's Research Collaborative on the Biology and Biophysics of RNP Granules (PRB, TM)
American Lebanese Syrian Associated Charities (TM)
Any opinions, findings, conclusions, or recommendations expressed in this material are those of the author(s) and do not necessarily reflect the views of the funding agency or any other bodies.

Author contributions:

Conceptualization: PRB, TM
Methodology: PRB, TSM, AB, XG, AS, JLB, TM
Investigation: all authors
Visualization: PRB, TSM, AB, XG, AS, JLB, TM
Project administration: PRB, TM
Supervision: PRB, TM
Resources: PRB, TM
Writing – original draft and revision: PRB, TM, TSM
Writing – reviewing and editing - all authors
Funding acquisition: PRB, TM

Competing interests: T.M. is a member of the advisory board of *Molecular Cell*. P.R.B. is a member of the *Biophysics Reviews* (AIP Publishing) editorial board. These affiliations did not influence the work reported here. All other authors have no conflicts to report.

Data and materials availability: All data are available in the manuscript or the supplementary materials. The scripts used for Thioflavin T kinetics and rheology data analyses in the current study are available on GitHub (see github.com/BanerjeeLab-repertoire/Interface-density-and-viscoelasticity-of-heterotypic-condensates-determine-their-ability-to-suppress).

Supplementary Materials

Materials and Methods
Figs. S1 to S8
Supplementary Notes
Tables S1 to S5
References (55 - 61)
Captions for Videos S1 to S6
Videos S1 to S6